nature communications

Article

https://doi.org/10.1038/s41467-026-70902-5

# Versatile water-floated nanostructures for three-dimensional nanotransfer printing

Received: 13 March 2025

Accepted: 6 March 2026

Published online: 30 March 2026

Check for updates

Byung-Ho Kang[1,2], Ji-Hwan Ha[3], Yeongjae Kwon[1], Sohee Jeon[2,4], Donho Lee[1], Byeongmin Kang[1,2], Soon Hyoung Hwang[2], Junseong Ahn[5] ✉, Jun-Ho Jeong[2,6] ✉ & Inkyu Park[1] ✉

Integrating functional nanostructures onto diverse three-dimensional surfaces is important for a wide range of applications, including holography, sensors, and extended reality. Nanotransfer printing (nTP) has emerged as a leading approach owing to its high throughput and resolution. However, conventional nTP techniques often require toxic solvents, adhesives, or thermal treatments, which limit the range of compatible substrates. Here, we introduce a water-floating-based nanotransfer printing (WF-nTP) technique inspired by hydrographic printing. In WF-nTP, nanostructures are floated on water and transferred onto target substrates via a scooping process. WF-nTP enables conformal transfer of Au, Pt, Pd, and Ni nanomeshes onto diverse substrates, including curved optical lenses, fibers, and plant leaves with micro-/nanoscale roughness. The technique also supports transfer onto hydrophobic surfaces by modulating the surface tension of the water bath. To highlight process versatility, two representative applications are demonstrated: the fabrication of multilayer SERS nanomesh fabrication for pesticide detection and the integration of Pd nanomeshes onto electrospun fibers for sensitive hydrogen sensing. Overall, WF-nTP provides a straightforward, substrate-independent route for nanostructure transfer with broad potential in advanced sensing and display technologies.

The rapidly advancing field of next-generation nanotechnology is gaining considerable attention as it seeks to implement nanostructures on various two-dimensional and three-dimensional (3D) surfaces, expanding the range of applications in various areas, such as chemical[1–3] and physical sensors[4–6], metamaterials[7], optical devices[8,9], and surface-enhanced Raman scattering (SERS)[10–12]. Conventional techniques have been extensively employed to fabricate nanostructures on a variety of substrates. Bottom-up approaches, such as self-assembly[13], chemical vapor deposition (CVD)[14], atomic layer deposition (ALD)[15], are effective for synthesizing nanomaterials at the atomic or molecular level. However, they often require material- and substrate-specific processing conditions such as high vacuum pressure, high temperature, or toxic chemicals, which limit their flexibility for direct pattern transfer onto diverse substrates that are vulnerable to such conditions. By contrast, top down approaches, including e-beam lithography[16], focused-ion beam lithography[17], nanoimprint lithography[18], and nanotransfer printing (nTP)[19,20], enable the direct fabrication of pre-defined nanostructures onto a wide variety of target surfaces. Among these methods, nTP distinguishes itself through its cost-effectiveness, high throughput, high process speed, high spatial

[1]Department of Mechanical Engineering, Korea Advanced Institute of Science and Technology (KAIST), Daejeon, South Korea. [2]Nano Lithography and Manufacturing Research Center, Korea Institute of Machinery and Materials (KIMM), Daejeon, South Korea. [3]Department of Mechanical Engineering, Hanbat National University, Daejeon, South Korea. [4]College of Pharmacy, Chung-Ang University, Seoul, South Korea. [5]Department of Control and Instrumentation Engineering, Korea University Sejong, South Korea. [6]Department of Microbiology, College of Medicine, Chung-Ang University, Seoul, South Korea. ✉e-mail: junseong@korea.ac.kr; jhjeong@kimm.re.kr; inkyu@kaist.ac.kr

resolution, reliability, and ability to accommodate diverse materials and morphologies[21]. The fundamental mechanism of nTP relies on controlling interfacial adhesion forces between the mold, substrate, and target material[21]. Successful transfer of the patterned nanostructure to the substrate occurs when the adhesion force between the target material and mold ($F_{mold}$) is weaker than that between the target material and substrate ($F_{substrate}$); i.e., $F_{mold} - F_{substrate} < 0$. Two primary approaches are generally employed to facilitate nTP: enhancing $F_{substrate}$ or reducing $F_{mold}$. $F_{substrate}$ can be enhanced by adding an adhesive layer between the substrate and target material, exploiting the thermoplastic properties of the substrate[22,23], or using a nanowelding process[24,25]. However, this approach necessitates altering the inherent properties of the substrate by introducing additives, applying pressure, or increasing temperature, potentially compromising the preservation of the original substrate characteristics. Conversely, $F_{mold}$ can be reduced by lubricating the interface between the mold and target material with a solvent[19] or employing a mold dissolution process[3]. Although this strategy does not require excessive substrate deformation or adding extraneous materials, it often involves toxic solvents and additional steps to remove solvent-soluble layers. In addition, both approaches face challenges associated with the rigidity of the mold, which hinders conformal contact with substrates, particularly those with 3D curved surfaces. Consequently, the increasing demand for nanostructure transfer methods that are independent of substrate properties and avoid toxic or potentially damaging processes necessitates a simple and direct transfer technique that is well suited for curved surfaces.

This study proposes an nTP technique inspired by hydrographic printing. Hydrographic printing typically involves floating ink and transferring it onto a submerged object. Based on this process, the nanostructure is floated on water and transferred to a substrate through a “scooping up” process. This process can be performed in three stages, as shown in Fig. 1a. Figure 1a-i illustrates the proposed concept, which involves plasma etching a metal-deposited nanopatterned mesh mold, weakening $F_{mold}$. When immersed in water, the etched gaps generate vacancies, allowing water to penetrate and separate the mesh from the mold. Subsequently, the suspended mesh floats on the water (Fig. 1a-ii) and can be easily transferred to curved surfaces. As previously mentioned, the transfer mechanism is straightforward. Figure 1a-iii presents the mechanism for transferring nanostructures onto curved 3D substrates through the “scooping up” method. During the drying process, the progressive evaporation of water reduces the size of the liquid meniscus formed between the gold nanomesh and the substrate. This reduction in meniscus size leads to an increase in its curvature, thereby significantly enhancing the capillary forces that pull the mesh into intimate contact with the substrate and promote strong, short-range adhesion[26–29]. Once the water has completely evaporated, the mesh remains stably adhered to the substrate through van der Waals forces, which are maximized by the close contact established during the capillary-driven process. In other words, the capillary action serves to bring the nanomesh and substrate surfaces into exceedingly close proximity, thereby maximizing the van der Waals interaction. The versatility of water-floating nanotransfer printing (WF-nTP) has been demonstrated on various 3D substrates, such as curved optical lenses and plant leaves with micro/nanoscale roughness. The metal nanomesh conformed to these surfaces without defects. Notably, this technique allows transfer onto hydrophobic surfaces, including the backs of leaves, thermoplastic polyurethane (TPU) fibers, and superhydrophobic lotus surfaces, by adjusting the surface tension of the water bath. This method enables the transfer of nanostructures onto a wide range of substrates without requiring adhesives or additional energy.

The proposed WF-nTP technique offers significant advantages, particularly for transferring nano-scale materials onto curved surfaces. Unlike conventional hydrographic printing, which is restricted to macro-scale decorative patterns on water-soluble films such as PVA, our WF-nTP method enables the transfer of high-resolution nanoscale structures directly onto various substrates. This advancement eliminates the need for sacrificial PVA layers and chemical activators, significantly reducing process complexity and the risk of polymer residue contamination. For further comparison, the metal-independent nTP method proposed by Hwang et al. uses a self-assembled monolayer (SAM) layer and requires covalent bonding with an adhesive coating at temperatures of at least 150 °C to transfer metals onto flat and curved surfaces[30]. Miyamoto et al. developed a simpler approach using water-soluble polyvinyl alcohol (PVA) electrospun (ES) fibers as a sacrificial material, enabling the transfer of Au nanowires to various surfaces, including human skin, by washing the PVA with water[31]. However, this method relies on sacrificial layers that may introduce residue and process complexity. By contrast, the WF-nTP technique eliminates the need for adhesive layers, toxic solvents, thermal energy, or sacrificial materials, allowing the metal nanomesh to float directly on water and be transferred via a simplified, residue-free process. Therefore, the nanostructure can be easily transferred onto curved surfaces by simply scooping them in a water bath, making the process simpler and more versatile.

Using this versatile transfer technique, two representative applications were demonstrated, as illustrated in Fig. 1b. A surface-enhanced Raman spectroscopy (SERS) mesh was first demonstrated using multilayer nanomeshes. The optimal number of layers was confirmed through finite-difference time-domain (FDTD) simulations and validated using Raman spectra measurements of Rhodamine 6 G (R6G). For practical applications, the mesh was transferred onto a leaf and fruit for nondestructive pesticide detection. In addition, a Pd-based mesh was successfully transferred onto ES TPU fibers to create a hydrogen gas sensor. This sensor, benefiting from the ability of palladium to detect hydrogen gas through reversible transformation, maintained the gas permeability of the fiber even after the nTP process. Consequently, it demonstrated sensitive and reliable detection under a 1 % hydrogen concentration.

## Results

### Fabrication and various morphological analyses of the transferred nanostructures

Fabrication of the water floated Au nanomesh is illustrated in Supplementary Fig. 1. The Au-deposited polyurethane acrylate (PUA) mold was first prepared. A square-dot replica PUA mold was obtained from the square-mesh patterned master mold through a nanoimprinting process. Subsequently, Au-deposited the PUA mold was fabricated using e-beam evaporation. Supplementary Fig. 2 shows the photographic images on this process. For the nanomesh to float on water as illustrated in Fig. 2a, Au mesh was first separated from the PUA mold through selective plasma etching. Before plasma etching, the square dots were removed using a metal-independent nanotransfer printing technique developed by the authors’ group. This process successfully removed the upper square dots from the mold, as shown in Fig. 2b-i and Supplementary Fig. 3. Subsequently, the optimal plasma etching time was determined by examining its effects on the PUA mold. Notably, as shown in Fig. 2b-ii to b-iv, the width of the square dot region of PUA decreases with increasing etching time, reducing the adhesion force between the Au mesh and mold. Because PUA is more vulnerable to plasma than gold, the width of the PUA mold decreases with increasing etching time without damaging the Au. When the etching time exceeds 5 min, the Au mesh begins to suspend, with the mold fully collapsing after 20 min. Therefore, an optimal etching time of 20 min enables effective detachment of the Au mesh from the mold, as the adhesion force between them is nearly completely eliminated, weakening $F_{mold}$. This creates a vacancy between the mold and Au, allowing water penetration and facilitating the separation of the Au mesh from the mold when immersed in water. The minimum thickness

https://doi.org/10.1038/s41467-026-70902-5

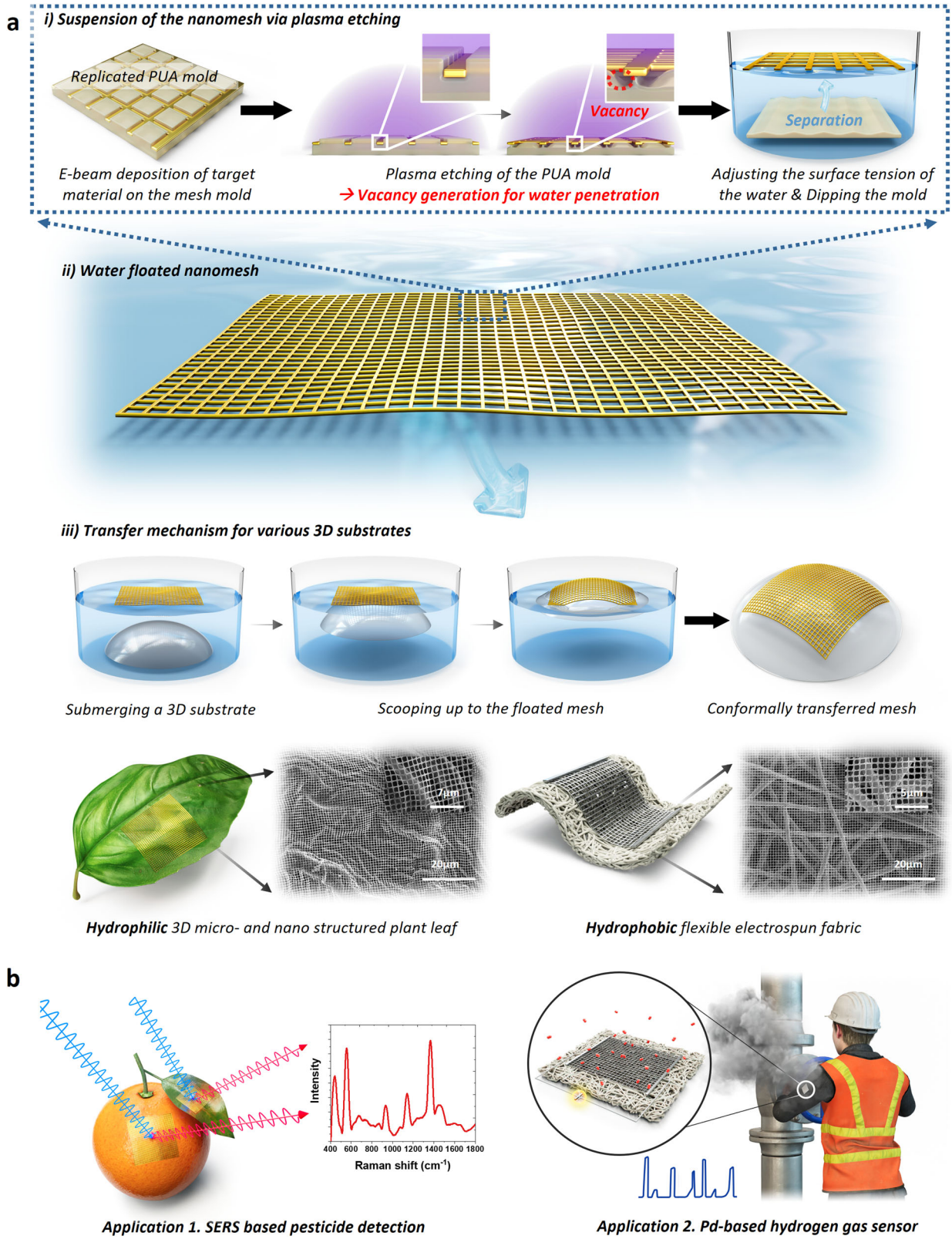



**Fig. 1 | Overview of the water-floated nano mesh and versatile transfer technique. a** The floating and transfer techniques are followed divided into three stages: i) suspension of the nanomesh through plasma etching, ii) formation of the water-floated nanomesh, and iii) transfer mechanism enabling application onto diverse 3D substrates, such as curved optical lense, hydrophilic plant leaf, and hydrophobic flexible electrospun fiber, demonstrating high versatility. **b** Versatile applications of the transferred nanomesh: SERS-based pesticide detection and Pd-based hydrogen gas sensor.

https://doi.org/10.1038/s41467-026-70902-5

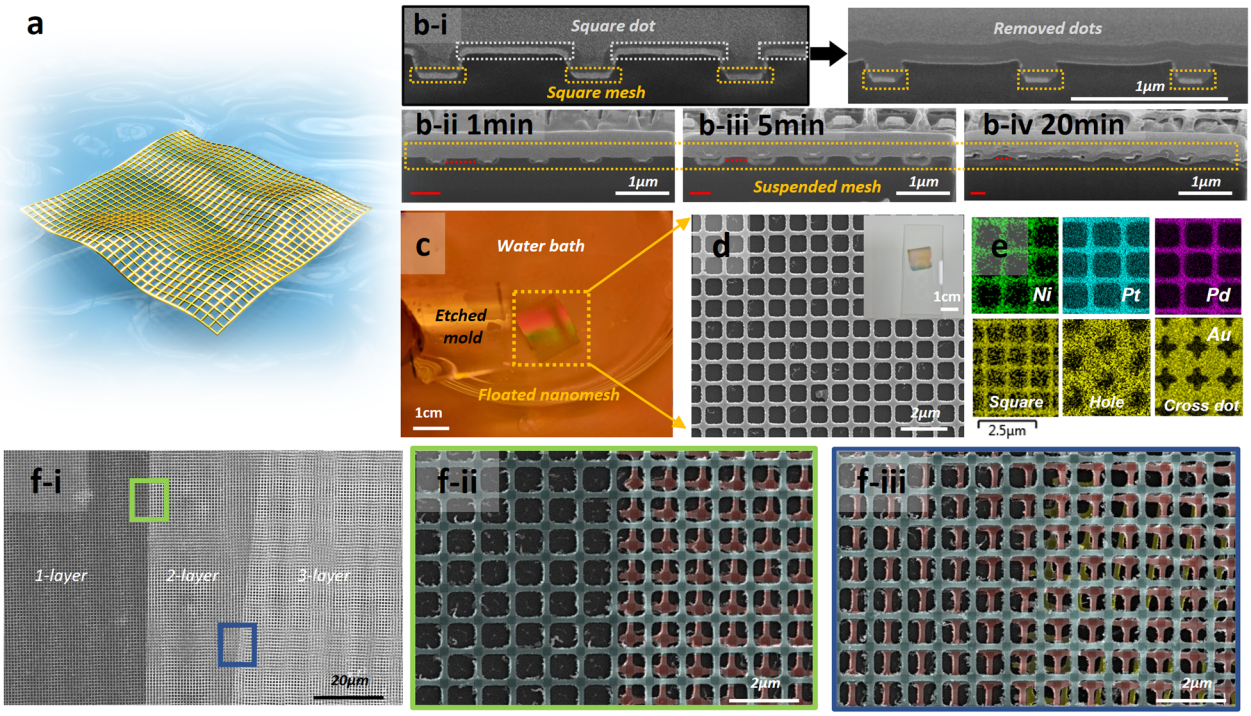



**Fig. 2 | Various morphological analyses of the floated nanostructure.** **a** Conceptual illustration of the water-floated nanomesh. **b** Cross-sectional images of the square dot and mesh mold with Au (depicted in gray- and orange-colored open rectangles), showing the dot removing procedure (b-i) and the effects of different etching times (b-ii to b-iv). The red line in each image indicates the width of the square dot region. **c** Photographic image of the water-floated nanomesh. **d** SEM image of the Au square mesh transferred onto slide glass, with the inset showing a photographic image of the square nanomesh on the slide glass. **e** EDS images of various metal meshes with different mesh patterns, demonstrating the versatility of the floating technique in transferred materials and mesh type diversity. **f** SEM images of the multi-layered mesh on slide glass (f-i); the green and navy boxes highlight the interfaces between the 1st and 2nd layers (f-ii) and the 2nd and 3rd layers (f-iii), respectively (dark green, violet, and yellow indicate the 1st, 2nd, and 3rd layers).

required for the mesh to stably float on water is 20 nm, allowing the ultrathin nanomesh to float on the water surface, as illustrated in Fig. 2c. Films thinner than 20 nm, particularly near 10 nm, exhibit severe embrittlement due to smaller grain size and reduced plastic deformation capacity. This results in a high density of cracks and brittle fractures during deformation[32], causing such thin films to hardly float on water. In contrast, 20 nm films retain sufficient ductility to withstand the floating and transfer process, establishing 20 nm as the practical lower limit for stable nanomesh flotation. Then, the mesh was transferred onto a slide glass for morphological analysis, confirmed through scanning electron microscopy (SEM) imaging, as shown in Fig. 2d. Figure 2e shows the energy-dispersive spectroscopy (EDS) mapping of various materials and mesh structures, highlighting the diversity of the materials and mesh configurations. Given that the WF-nTP process requires a plasma etching step, the choice of metals is limited to those resistant to oxidation. Notably, various oxidation-resistant metals, such as Ni, Pt, and Pd, along with different mesh patterns, such as holes and cross-dots, can also float on water and be transferred onto substrates. For successful and stable floating, the nanostructure must be laterally interconnected. Mesh-type geometries such as square mesh, hole arrays, cross-dot grids) maintain mechanical integrity on the water surface and prevent uncontrolled drifting. In addition, the WF-nTP technique enables multilayer stacking. Figure 2f shows the SEM images of a three-layer stack on a glass slide. Once the mesh fully dries after being lifted from the water bath, it remains stably attached to the substrate owing to capillary-driven strong van der Waals forces, even when submerged in water again. This high stability enables further nTP processes on pre-transferred substrates, allowing multiple mesh layers, rather than just a monolayer, to be transferred onto the desired substrate.

## Results of nTP on various 3D surfaces

To demonstrate the applicability of the developed nTP technique to 3D or curved surfaces, the Au mesh was transferred onto an optical lens with varying radii of curvature, as illustrated in Fig. 3a. Because WF-nTP does not require any adhesive or supporting substrate, the mesh coule be transferred onto a curved 3D surface simply by scooping it in water. The Au mesh was successfully transferred onto the curved surface regardless of the curvature radius. To verify the integrity of the mesh structure on the lens, an optical microscope (OM) was used to record a video (Supplementary Movie 1) while sweeping the focus across $R_6$, which is the most curved surface. Each region was individually scanned to assess the fine structure of the mesh. The video confirmed that the mesh retained its original structure across the entire lens surface. To further verify crack-free transfer on the lens, the electrical resistance at each edge point of the Au mesh was measured. Au meshes with thicknesses of 20, 40, 80, and 100 nm were transferred onto four lenses with different radii of curvature, and the resistance was measured by placing the probe in contact with the edge of each mesh, as shown in Fig. 3b and Supplementary Fig. 4. The results indicated that the electrical resistance remained consistent across lenses with the same Au thickness, confirming crack-free contact despite varying radii of curvature. As anticipated, the resistance decreased with increasing Au thickness in all cases.

The versatile WF-nTP method also demonstrates significant advantages when transferring nanostructures onto thermally and mechanically sensitive substrates, such as plant leaves. Considering the micro- and nanoscale roughness of plant leaves, including numerous curved surfaces, the versatility of WF-nTP was examined by applying it to a *Nandina domestica leaf*. Figure 3c shows a photographic image of the leaf with single-layer and three-layered Au

https://doi.org/10.1038/s41467-026-70902-5

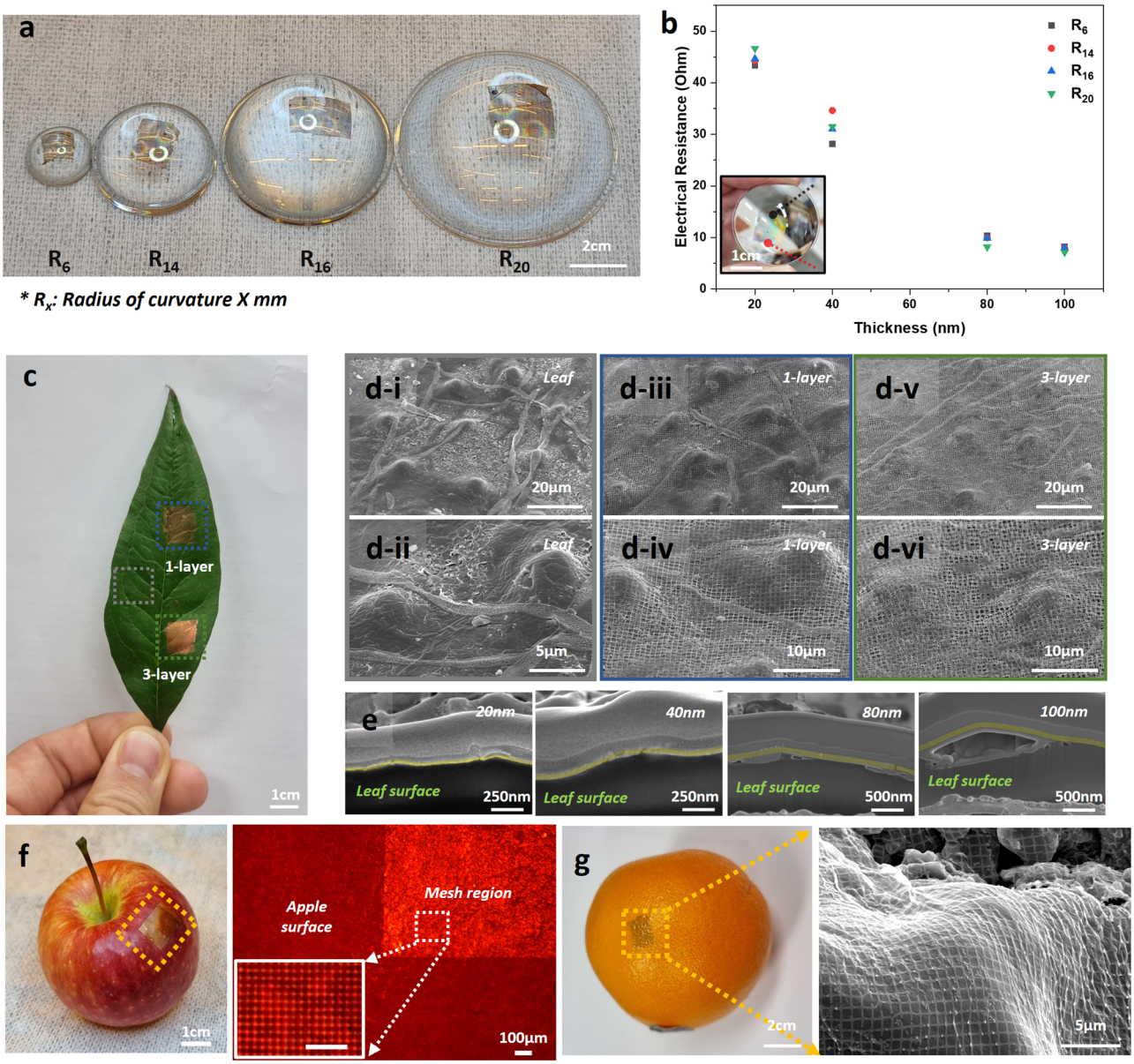



**Fig. 3 | Results of nTP on various 3D surfaces and morphological analysis.** **a** Photographic image of the nanomesh on a curved optical lens with varying radius of curvature. **b** Electrical resistance of the nanomesh on the lens as a function of Au thickness. The resistance was measured by contacting the multimeter tip to the edge of the mesh, as shown in the inset. **c** Photographic image of the Au mesh on a leaf. **d** SEM images of the raw leaf surface (d-i) and (d-ii), a 1-layer mesh on the leaf (d-iii) and (d-iv), and a 3-layer mesh on the leaf (d-v) and (d-vi). **e** Cross-sectional image of the 1-layer mesh on the leaf, showing the variation in Au thickness. **f** Photographic and OM images of the nanomesh on an apple. Inset image shows the magnified OM image of the mesh region (scale bar: 100 μm) **g** Photographic and SEM images of the nanomesh on orange.

meshes. SEM analysis was performed to compare the morphological characteristics of the mesh on the leaf, beginning with the raw leaf surface, as shown in Fig. 3d-i and d-ii. The raw leaf surface exhibited rough textures and irregular curvature distributions. However, upon transferring the Au mesh, it conformally adhered to the rough surfaces of the leaf without significant defects, as presented in Fig. 3d-iii and d-iv. The surface tension and capillary force during the drying process facilitated this successful adhesion, enabling the Au mesh to firmly adhere to the surface. In addition, multilayer stacking was achieved on the leaf, even over the curved regions, as shown in Fig. 3d-v and d-vi. Relatively low magnification SEM images are also presented in Supplementary Fig. 5a–c to demonstrate that a large area could be covered. To further validate the conformity of the mesh to the leaf surface, cross-sectional images showing different mesh thicknesses were obtained, as shown in Fig. 3e. The yellow line represents the Au mesh, which conformally follows the original contours of the curved leaf surface. To quantify the bending radius corresponding to the elastic limit of the mesh structure, we performed COMSOL simulations on a single unit cell of the mesh. The detailed simulation methods are provided in Supplementary Methods part. From the simulation, the bending radius corresponding to the elastic limit for the 20 nm thick Au mesh was estimated to be approximately 800 nm, as shown in Supplementary Fig. 6. However, it is important to note that this result reflects only the local mechanical behavior of an individual unit cell and does not fully capture the characteristics of the entire mesh, which is composed of an array of such cells. To better understand the practical bending behavior, we analyzed the cross-section of the plant surface shown in Fig. 3e through image processing to calculate

curvature and radius of curvature (Supplementary Fig. 7). This analysis revealed that the smallest radius of curvature on the plant surface was about 280 nm. Interestingly, the Au mesh was able to conformally bend over surfaces with radii of curvature smaller than the bending radius corresponding to the elastic limit estimated by the single unit cell simulation. This observation indicates that the array architecture of the mesh imparts greater flexibility than what is predicted by the unit cell model alone, enabling the mesh to adapt to highly curved surfaces more effectively. Furthermore, even when the local radius of curvature of the plant surface is below 300 nm, the Au can still be transferred without fracture due to its intrinsic ductility and ability to undergo local plastic deformation. As a result, the 20 nm-thick Au mesh maintains overall mechanical integrity and conformability through plastic deformation rather than purely elastic deformation, enabling successful transfer even on surfaces with curvatures sharper than the theoretical elastic limit. In the case of 3-layer mesh as depicted in Supplementary Fig. 5d, 3 layers of mesh also conformally formed along the original surface. Beyond morphological analysis of conformal contact on the leaf, electrical impedance spectroscopy (EIS) was also conducted, as shown in Supplementary Fig. 8. Since biological surfaces such as plant leaves exhibit both resistive and capacitive behavior, EIS is more suitable than simple surface resistance measurements. It provides information on electrical properties of both the surface and internal structure including moisture content and ion distribution, therefore EIS is widely used to monitor plant health[33]. Given that stable and clear impedance measurements require electrodes to conform closely to the surface, we compared a conventional clip electrode with a single-layer Au mesh electrode transferred via WF-nTP. Both showed stable signals over a broad frequency range (1 to $10^5$ Hz), but the Au mesh consistently exhibited lower impedance at all frequencies, as shown in Supplementary Fig. 8a. In phase angle spectra, the clip electrode showed some noise, whereas the Au mesh produced very clear signals, as provided in Supplementary Fig. 8b. These results demonstrate that the Au mesh produced by WF-nTP was conformally transferred onto the plant surface. In addition, the stability of the mesh on the leaf was assessed by comparing its surface morphology before and after showering (Supplementary Movie 2). During the showering process, the yellow mesh preserved its original structure without cracks. To confirm this result at the microscopic level, SEM analysis was performed on the 1-layer mesh before and after showering, as shown in Supplementary Fig. 9. Notably, no significant defects or damage such as large holes, fractures, or distortions were observed after showering, indicating that the mesh was robust and firmly adhered to the leaf. While minor defects typical in ultrathin nanostructure on rough natural surfaces may exist, these did not affect the overall structural integrity or electrical performance of the mesh. These results confirm that the WF-nTP method is particularly advantageous for transferring various functional nanopatterned metals onto rough surfaces, demonstrating excellent mechanical stability even under strong water exposure. To further demonstrate the versatility of the WF-nTP technique, apple and orange substrates were used for transfer. Figure 3f shows photographic and optical microscopy (OM) images of the apple with the transferred mesh. The faint yellow square indicates the successfully transferred mesh, as verified by the OM images. The brighter region represents the mesh, and the inset shows a magnified view, confirming its structural integrity. Similarly, Fig. 3g shows photographic and SEM images of the mesh on an orange, further demonstrating the broad applicability of this method.

### Results of nTP on various hydrophobic surfaces

The wetting properties of the target substrate with the liquid in the bath are critical to the WF-nTP process. In the previously discussed experiments using water as the transfer medium, WF-nTP was successfully performed on hydrophilic surfaces, such as glass slides and the front side of the leaf. However, challenges may arise when transferring nanostructures onto hydrophobic surfaces. For instance, the back side of the *Nandina domestica* leaf is hydrophobic, as illustrated in Supplementary Fig. 10. The contact angle on the back side of the leaf exceeds 90 °, with a significantly higher roughness compared with the glass slide and the front side of the leaf, both of which have contact angles below 90 °. When the contact angle exceeds 90 °, nTP cannot be implemented because the repellent force of the liquid prevents mesh transfer. To address this challenge, the transfer medium (i.e., liquid in the bath) must be strategically adjusted. The contact angle between the substrate and liquid depends on the vapor above the free surface of the liquid, as well as the nature of the liquid and solid in contact. In this experiment, because the substrate and vapor layer are fixed variables, the contact angle can be reduced by altering the liquid, specifically by adjusting its surface tension. Water, which has a relatively high surface tension compared with many other liquids, is not an ideal transfer medium for hydrophobic surfaces. However, mixing ethanol with water significantly reduces the surface tension of the solution[34]. This reduction in surface tension enables the modification of the contact angle on the back side of the leaf. Figure 4a shows the contact angles of different solutions with varying ethanol-to-water volume ratios. As the ethanol volume fraction increases, the contact angle decreases, indicating improved wettability on the back side of the leaf.

Based on these findings, the Au mesh was floated on each solution. The reduced contact angle enabled the successful transfer of the Au mesh onto the hydrophobic surfaces. However, when the ethanol volume fraction exceeded 30%, the Au mesh could no longer float on the surface of the solution owing to the excessively low surface tension[34]. This indicates that a specific surface tension is necessary to float the target materials and wet the substrate at low contact angles. The optimal liquid medium composition for hydrophobic surfaces was determined to be an 80/20 (v $v^{-1}$) water/ethanol mixture, exhibiting a surface tension of approximately 42.9 mN $m^{-1}$ [34]. Subsequently, the Au mesh was transferred onto the back side of the leaf using the optimized water/ethanol mixture. As shown in Fig. 4b, the mesh conformally adhered to the hydrophobic surface without cracks or fractures.

To further verify the versatility of the substrate, ES TPU fibers were fabricated and used as another example of a hydrophobic surface[23]. As shown in Fig. 4c, the contact angle variation with changing ethanol-to-water volume ratios exhibited a similar trend for the ES TPU fibers. Figure 4d shows the successful transfer of the Au mesh onto the fibers. To further validate conformal transfer, a cross-sectional image is shown in Supplementary Fig. 11. Conventional nTP methods for thermoplastic substrates such as TPU typically require thermal energy and high pressure, potentially damaging and deforming the substrate. However, the WF-nTP was successfully implemented without the need for thermal energy or pressure. Finally, the Au mesh was successfully transferred onto a lotus leaf, known for its superhydrophobic properties[35], by adjusting the liquid medium composition. Figure 4e presents the variation in the contact angle of the lotus for each mixture with OM images depicting water droplets exhibiting high contact angles on the lotus leaf. However, when water was replaced with a water/ethanol mixture, the lotus leaf became wettable, and the Au mesh was successfully transferred onto the lotus surface. Supplementary Fig. 12 shows the photographic image of lotus with water droplet on the leaf. The lotus surface is composed of complex hierarchical pillar structures that contribute to its super-hydrophobicity, as shown in Fig. 4f [36,37]. Despite its structural complexity and superhydrophobicity, the Au mesh conformed to the surface through the developed WF-nTP. Relatively low-magnification SEM images of the lotus leaf with and without the Au mesh are shown in Supplementary Fig. 13. This demonstrates that the substrate-independent WF-nTP technique is a universal and straightforward method for transferring metal nanostructures across various surfaces.

https://doi.org/10.1038/s41467-026-70902-5

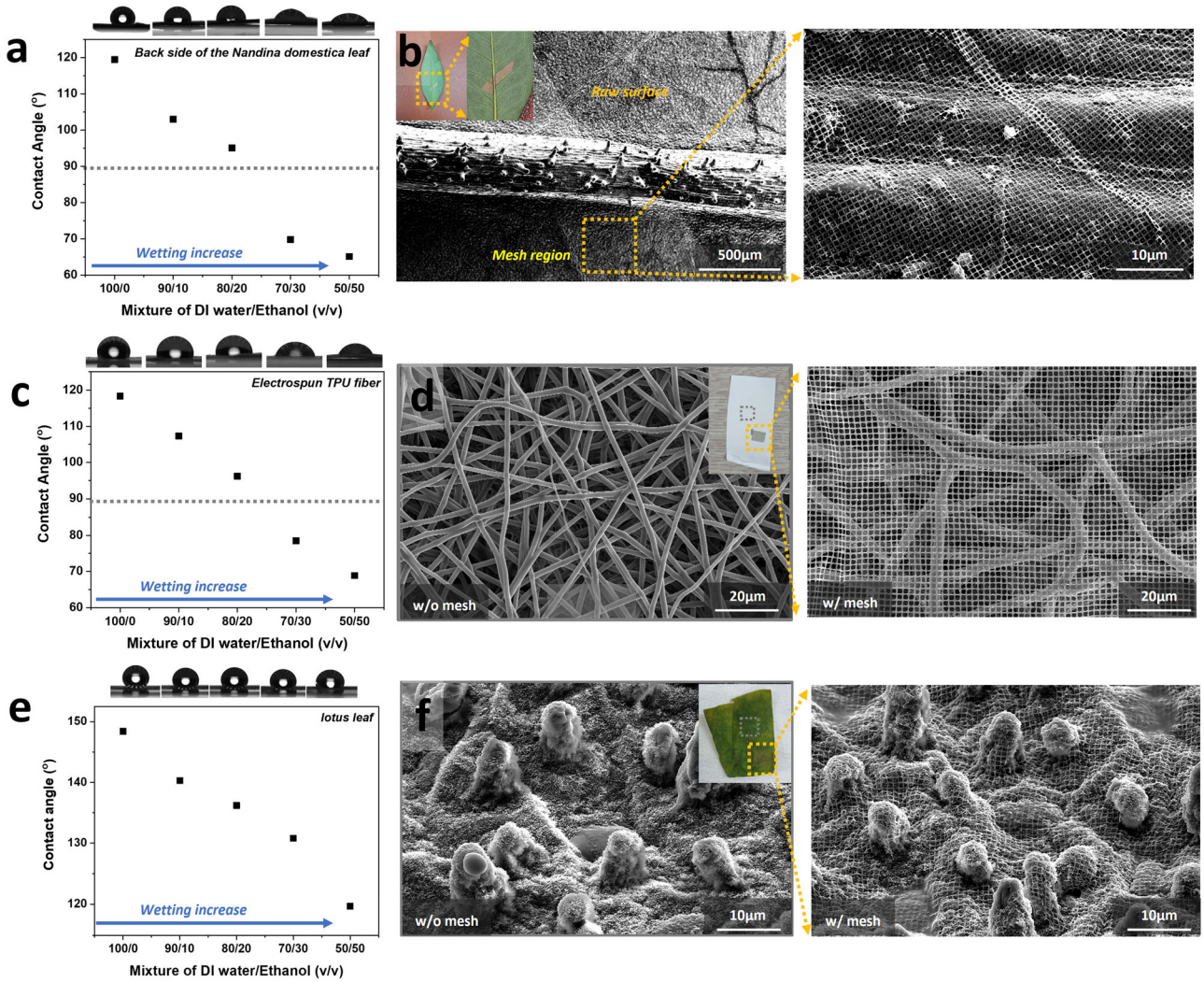



**Fig. 4 | Transfer to hydrophobic surfaces and morphological analysis. a** Contact angle measurements on the back side of the *Nandina domestica* leaf using different volume ratios of DI water and ethanol. **b** SEM images of the Au mesh on the back side of the leaf, showing conformal contact with the rough surface. **c** Contact angle measurements on the electrospun TPU fiber using different volume ratios of DI water and ethanol. **d** SEM and photographic images (inset) of the Au mesh on hydrophobic electrospun TPU fibers. **e** Contact angle measurements on the lotus leaf using different volume ratios of DI water and ethanol. As ethanol content increases, the contact angle decreases, indicating improved wetting properties on the lotus leaf surface. **f** SEM and photographic images (inset) of the raw lotus surface and the transferred Au mesh on the lotus leaf.

## Design and demonstration of a SERS device for pesticide detection

A significant advantage of the WF-nTP method is its ability to facilitate multiple stacking of nanostructures on versatile substrates. Once the mesh is transferred and dried, it stably adheres to the substrate without detaching, enabling repeated transfers. Stacking several nanomeshes creates numerous hot spots for SERS between the layers. Figure 5a shows two representative hotspot types: horizontal and vertical. When the square meshes are stacked, gaps are formed in the horizontal and vertical directions, particularly for more than three layers. Although the positions of the horizontal gaps are uncontrollable owing to the random orientation during WF-nTP, this randomness can still generate numerous horizontal nanogaps. By contrast, the vertical gaps are easily controlled because they correspond to the thickness of each layer. Gaps with sizes less than 100 nm, particularly under 20 nm[38], can serve as hotspots for SERS. The thinnest stable Au mesh that can float on water is 20 nm thick, making it ideal for this application. The optimal number of layers for SERS was determined through FDTD simulations. The detailed simulation methods are provided in Supplementary Methods part. Figure 5b shows a 3D schematic of the multilayered nanomesh used in the simulation. The mesh units are stacked along the z-axis, and the laser wave is polarized along the x-axis. A 2D monitor was placed in the x-z plane across the layers. As shown in Fig. 5c, the maximum e-field enhancement increases with up to seven layers, creating three distinct vertical gaps along each vertical line. The major local enhancements occur between the topmost and third layers (first vertical gap), particularly between the third and fifth layers (second vertical gap). However, when the number of layers increases to nine, the maximum e-field enhancement decreases compared with that in the seven-layer configuration, as shown in Fig. 5f. This reduction can be attributed to the diminished ability of the laser to effectively penetrate the uppermost layers. In addition, the inconsistent e-field enhancement can be attributed to wave interference as it propagates through the multiple stacked layers. This interference can be either constructive or destructive, leading to a nonuniform distribution of e-field enhancement across the mesh structure[10]. Consistent with the literature on multi-stacked nanostructures for SERS[10], a two-layer stack can sometimes show a lower

https://doi.org/10.1038/s41467-026-70902-5

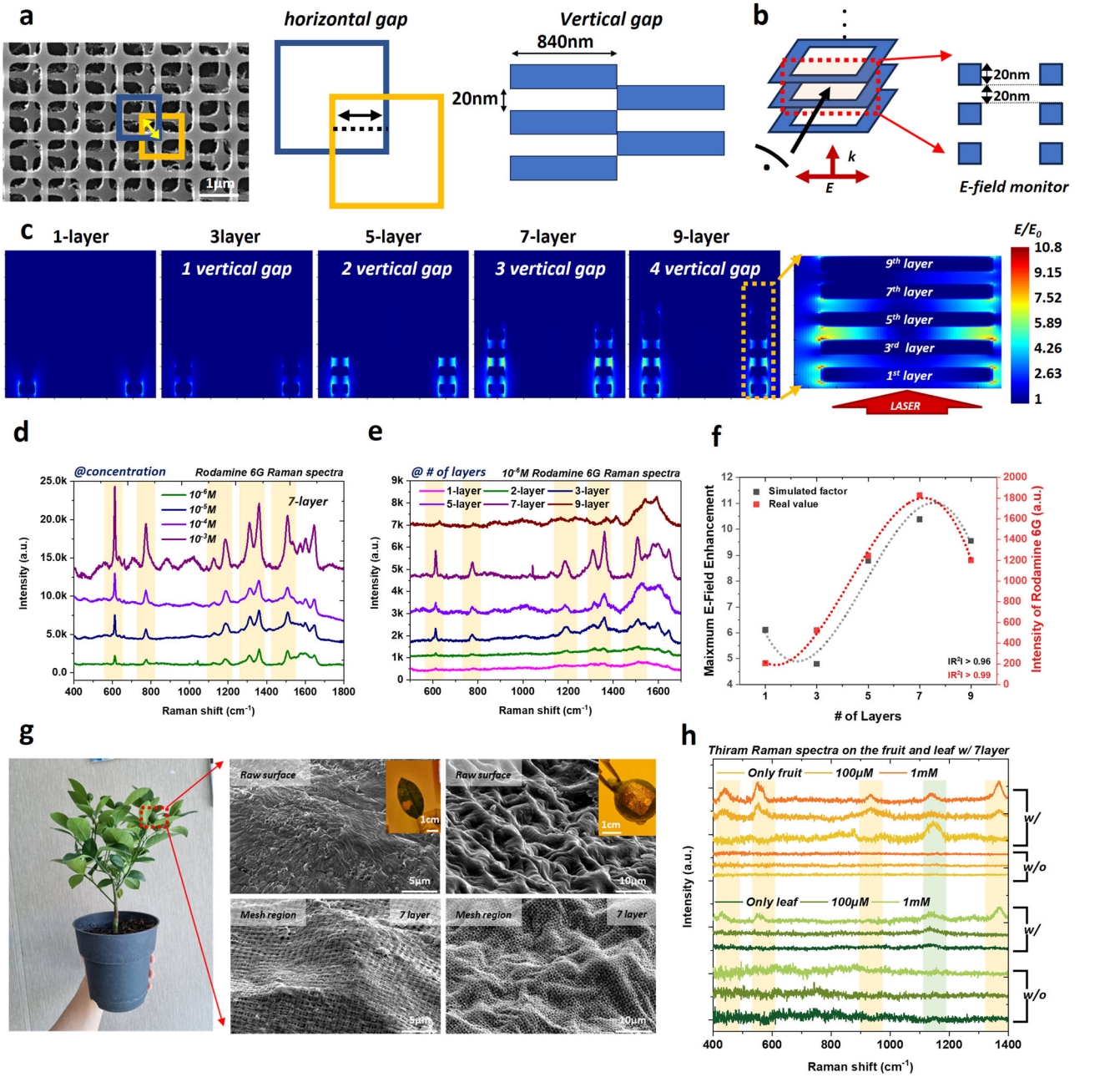



**Fig. 5 | Design and demonstration of a SERS device for pesticide detection.** **a** SEM image and schematic illustration showing two representative types of hot spots generated in the multi-layered mesh structure, and **b** geometry setup for FDTD simulation. **c** Simulation results for the multi-layered structure as a function of the number of stacking layers. **d** Raman spectra of R6G at concentrations ranging from $10^{-3}$ M to $10^{-6}$ M on the slide glass with a 7-layer mesh. **e** Raman spectra of $10^{-6}$ M R6G as a function of the number of layers. The yellow shade highlights the characteristic Raman shift peak of R6G. **f** Maximum E-field enhancement ($E/E_0 \geq 1$) of the multi-layered structure and the relative SERS signal intensity at ~1510 $cm^{-1}$ for $10^{-6}$ M R6G with polynomial fitting. **g** Photographic image of a lemon-orange tree, and SEM images of the leaf and fruit with and without the 7-layered Au mesh. **h**, Raman spectra of thiram on the leaf and fruit at different concentrations of thiram, with and without the mesh. The yellow shade highlights the characteristic Raman signal of thiram, while the green shade indicates that of the raw leaf and fruit.

maximum enhancement than a single layer because additional interfaces introduce destructive interference. Our three-layer calculation exhibits the same trend, resulting in a smaller e-field enhancement than the single-layer case. To assess the robustness of this conclusion against horizontal layer alignment, additional FDTD calculations for four representative in-plane registries between adjacent meshes across 2 to 9 layers were performed, with detailed results shown in Supplementary Fig. 14. Given that the possible combinations of alignment cases are unlimited, we cannot simulate every possible alignment configuration. Therefore, we performed simulations for several representative and limited scenarios. We believe these simulations adequately capture the overall trend observed in the multi-layer stacking effects on hot spot distribution and field enhancement. As a result, while horizontal misalignment redistributes the hotspot locations, the maximum e-field enhancement still displays a clear optimum near 6 to 7 layers, consistent with the trends observed in Fig. 5c and f. This suggests that the layer-dependent optimum is determined primarily by the interplay between vertical coupling and field attenuation from multiple interfaces, rather than any specific in-plane alignment. It should be noted that a direct one-to-one

correspondence between simulated enhancement and measured SERS intensity is not expected. The experimental measurement integrates signals from both horizontal and vertical hotspot arrays within a finite illuminated area. These factors, together with finite optical attenuation through the upper layers, explain why the simulated three-layer case can yield a lower maximum e-field enhancement than the single layer while the experimental Raman intensity for three layers can differ from the trend of the idealized vertical gap model. Despite these complexities, the overall behavior aligns with the previous study[10] and our supplementary alignment study in Supplementary Fig. 14, supporting the conclusion that an optimal layer count of approximately seven exists for the present mesh geometry.

Directly correlating these results with the experimentally measured SERS intensity is complex owing to the integrated effect of various hotspots (horizontal and vertical gap arrays). However, the overall trend can be compared[10]. The Raman signal of R6G, a representative material for SERS substrate evaluation, was measured on a glass slide with a seven-layer mesh, as shown in Fig. 5d[39–41]. R6G was detected at concentrations ranging from $10^{-3}$ M to $10^{-6}$ M using the seven-layer mesh. To evaluate the uniformity of the Raman signal across the substrate, measurements were taken at six different points on the mesh surface for each concentration. As shown in Supplementary Fig. 15, the Raman spectra obtained at these multiple locations exhibited consistent peak patterns and intensities, indicating a uniform signal distribution. The Raman signal of $10^{-6}$ M R6G was also measured as a function of the number of layers, as shown in Fig. 5e. Notably, the Raman intensity of R6G increased up to the seven-layer mesh but decreased with the nine-layer mesh, consistent with the simulated values. Figure 5f also illustrates that the trend in the SERS intensity as a function of the number of layers is consistent with the simulation results, although minor discrepancies are noted in the three-layer configuration. This suggests that a seven-layer mesh is the optimal condition for SERS in a 20 nm Au mesh system.

For practical applications, a seven-layer Au mesh was transferred onto the leaf and fruit of a lemon-orange tree for pesticide detection, as shown in Fig. 5g. The meshes conformed well to the surfaces of both substrates. Because leaves and fruits are sensitive to high temperatures and pressures, the WF-nTP method offers significant advantages for these applications. This technique enables direct and rapid printing without damaging the surface, enabling the simple and nondestructive detection of pesticides on leaves and fruits using SERS[42–46]. This study used thiram (tetramethylthiuram disulfide), a commonly used pesticide, for demonstration purposes. Detecting thiram residues on fruits is crucial because they pose health risks to humans. For this purpose, 1 mM and 100 μM thiram solutions in water were drop-cast over a 1 $cm^2$ area on the leaf and fruit. Figure 5h shows the characteristic Raman spectra of thiram on the leaf and fruit. Notably, without the seven-layer mesh, no characteristic thiram peaks are detected on either the raw leaf or fruit. However, after applying the seven-layer mesh, the peaks are observed in both cases. With the seven-layer mesh, the characteristic carotenoid peak in the raw fruit and leaf are detected at 1154 $cm^{-1}$, attributed to C–C stretching, while no significant peaks are observed in the raw cases[47]. For thiram, four characteristic peaks are identified in the fruit and leaf samples. The peaks at 437 and 560 $cm^{-1}$ corresponded to C = S and S–S stretching, respectively. In addition, the peaks at 928 and 1386 $cm^{-1}$ are attributed to C = S and C–N stretching[48,49]. These results indicate that the seven-layer mesh effectively enhanced the Raman signal. Notably, the detection limits varied between the leaf and fruit: 1 mM and 100 μM for the leaf and fruit, respectively. This discrepancy can be attributed to the more complex surface morphology and curvature of the fruit, which can create additional hot spots for SERS, as shown in Supplementary Fig. 16. These results indicate that the seven-layer Au meshes enhance the SERS signal, and surface morphology plays a crucial role. According to the EU pesticides database[19], the permissible pesticide residue levels for humans range from 22 μg $cm^{-2}$ to 31 μg $cm^{-2}$. The maximum detection limit for thiram on the leaf was 1 mM; however, the calculated amount was 6.49 μg $cm^{-2}$, five times lower than the permissible level. Therefore, the WF-nTP method demonstrates significant potential for application in SERS devices, particularly in the agricultural industry.

### Demonstration of Pd-based hydrogen gas sensor

To demonstrate the versatility of the WF-nTP process, a Pd mesh was transferred onto an ES TPU fiber substrate and used as a hydrogen gas sensor. ES TPU fibers are widely used for their suitability for creating stretchable masks and sportwear and their ease of integration into commercial clothing, enabling the creation of smart fabrics. In addition to the existing functions of ES fiber-based smart fabrics, such as hypoglycemia and diabetes diagnosis[23], wound monitoring, and healing[50,51], the WF-nTP technique has been employed to create Pd-based hydrogen gas sensors on TPU fibers. When Pd is exposed to hydrogen gas, it undergoes a reversible transformation into palladium hydride ($PdH_x$), increasing electrical resistance[3]. This change in resistance provides a straightforward mechanism for detecting hydrogen gas. Figure 6a schematically illustrates the structure of the Pd-based hydrogen gas sensor formed on electrospun fibers, showing how the mesh interacts with incoming hydrogen molecules. Figure 6b presents a photographic image of the sensor placed inside the gas-testing chamber along with a corresponding SEM image, confirming the morphology and integration of the Pd mesh with the fiber substrate. In this study, the relative change in the sensor resistance was tested for hydrogen gas concentrations ranging from 0.25 % to 1 %. As shown in Fig. 6c, the sensor response increases with the hydrogen gas concentration, with the relative resistance of the Pd mesh reflecting these changes. The gas sensor benefits from the stable transfer of the thin 100 nm Pd nanomesh, which enhances sensor sensitivity, and the sufficient permeability of the TPU fibers to hydrogen gas, enabling rapid gas absorption and desorption. This combination enables the clear detection of hydrogen concentrations below 1%. To further validate the stability and repeatability of the sensor, a 50-cycle test was performed for each concentration. As shown in Fig. 6d, the sensor demonstrates consistent responses with minimal variation, indicating the stable transfer of the Pd mesh onto the ES TPU fibers using WF-nTP. Finally, the gas selectivity of the sensor was evaluated by exposing it to various gases, including carbon monoxide (CO), hydrogen sulfide ($H_2S$), and nitrogen dioxide ($NO_2$), at different concentrations. As shown in Fig. 6e, the sensor exhibits negligible responses to these gases, at concentrations exceeding those permitted by the Occupational Safety and Health Administration (OSHA) guidelines[3]. These results confirm that the Pd-based sensor has superior selectivity for hydrogen gas over other potential interference gases, as provided in Supplementary Fig. 17. These findings suggest that the proposed WF-nTP process has significant potential for applications in the gas sensor field and the development of smart fabrics.

## Discussion

A straightforward and versatile water-floating nanotransfer printing (WF-nTP) technique applicable to curved 3D and hydrophobic surfaces was developed. By weakening the adhesion force between the mold and metal mesh through selective plasma etching, the mesh was suspended on the mold, allowing water to penetrate underneath. The suspended metal mesh was floated on the water surface and transferred by simply scooping it onto the desired substrate. This method proved effective for floating various metals, such as Au, Pd, Pt, and Ni, and transferring different mesh patterns, including hole and cross-dot designs. Notably, once the water residue on the substrate fully dried after scooping, the nanomesh stably adhered to the substrate, even when submerged in water repeatedly, enabling multilayer stacking. This straightforward technique facilitated the successful transfer of

https://doi.org/10.1038/s41467-026-70902-5

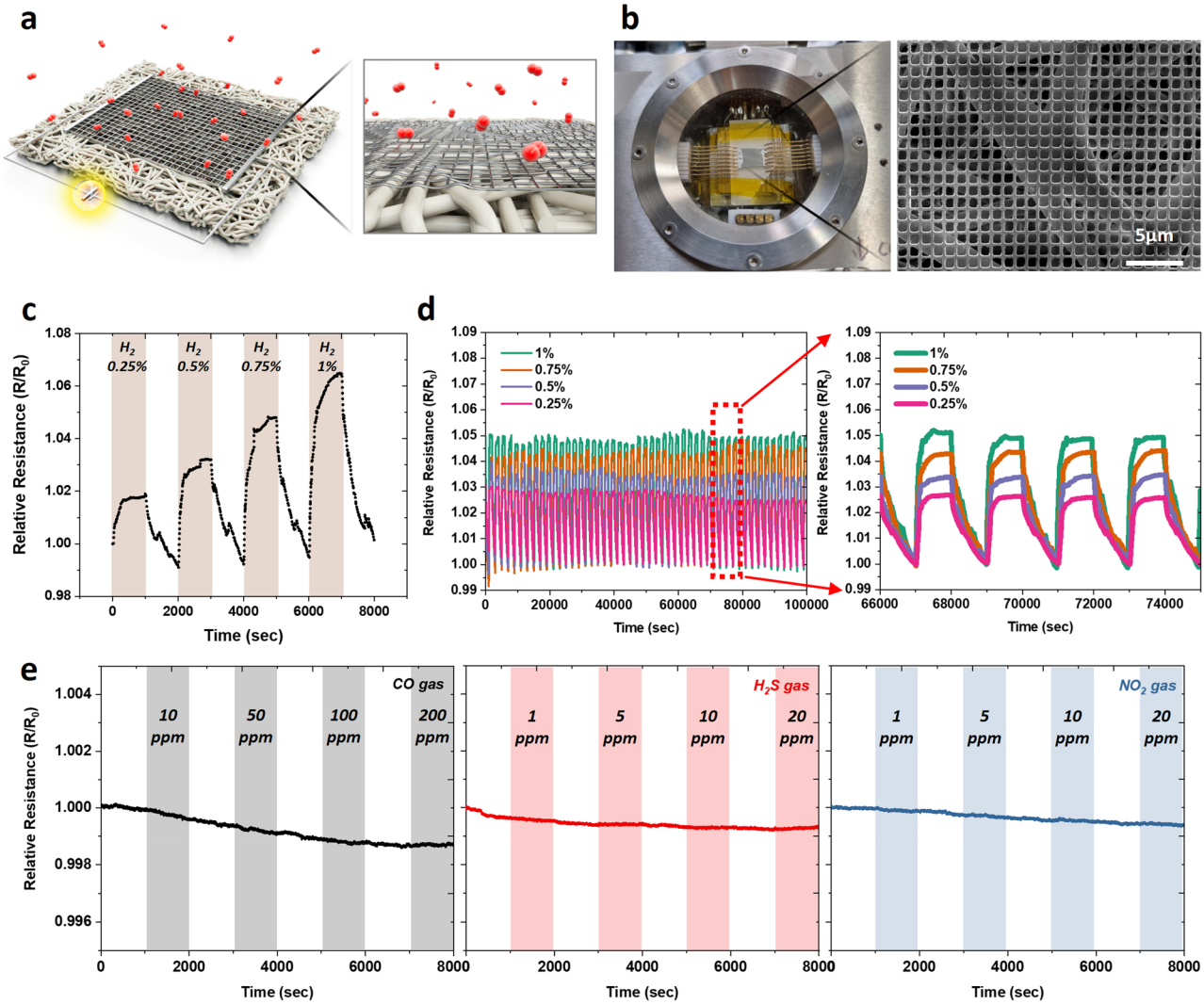



**Fig. 6 | Demonstration of Pd based hydrogen gas sensor. a** Schematic illustration of the Pd-based hydrogen gas sensor on an ES fiber. **b** Photographic image of the sensor inside the gas chamber, accompanied by an SEM image. **c** Response of the hydrogen sensor as a function of gas concentration. **d** 50-cycle test at each concentration demonstrating the sensor's stability and repeatability. **e** Gas selectivity for different gases, including CO, $H_2S$, and $NO_2$, at varying concentrations.

the nanomesh onto various curved surfaces and the creation of a multilayered nanomesh. Furthermore, the nanomesh was transferred onto hydrophobic surfaces by adjusting the surface tension of the liquid medium in the nTP bath, enabling its transfer onto superhydrophobic surfaces, such as lotus leaves. The versatility of the WF-nTP technique was demonstrated through two practical applications. First, a SERS mesh was developed using a multilayer stacking procedure. The optimal number of layers for achieving the highest e-field enhancement was determined through FDTD simulations and confirmed by experimental results. The seven-layer mesh provided the best conditions for SERS and was successfully applied for pesticide detection on fruits and leaves. This trend closely matches previous results reported for nanowire-based SERS substrates[10], where optimal enhancement was also achieved at a moderate stacking number. While the specific optimal layer differs due to structural differences, both studies demonstrate that there exists an optimal stacking condition maximizing SERS performance. Subsequently, a Pd-based hydrogen sensor was fabricated on ES TPU fibers. The Pd mesh was conformally transferred onto the ES fibers while preserving the intrinsic properties of the substrate. The sensor demonstrated the ability to detect low concentrations of hydrogen gas with excellent repeatability and significant selectivity over other interfering gases.

Despite the versatility of this transfer technique, further improvements are necessary to enhance its adaptability. A key requirement for successfully floating nanostructures on water is the use of a mesh-patterned mold. Unconnected patterns, such as lines or dots, cannot maintain their original structure when floated on water, causing them to disperse on the water surface. However, incorporating a sacrificial layer into these patterns can address this structural limitation. A heterogeneous 3D structure combining the line pattern and sacrificial layer can be created by bonding a layer of material sensitive to etchants or other removal substances onto the initial line pattern. Provided that the 3D structure can float on water, it can be transferred onto curved substrates. Subsequently, an additional treatment to remove the sacrificial layer is required to leave only the line pattern on the substrate without structural misalignment. Following this process, complex line patterns such, as circuit patterns, can be transferred onto the substrate using the WF-nTP technique.

For multi-layer stacking applications, a precise stacking technique should be developed. In our system, the alignment of all layers was

uncontrollable since they were stacked manually. However, inverting the stacking sequence can address the alignment issue. In the original approach, the nanostructure was first floated on water and then transferred onto the target substrate. This process was repeated to stack multiple layers. Alternatively, pre-stacking multiple layers to fabricate a 3D nanostructure prior to the transfer step can be a viable solution. Several strategies for fabricating 3D nanostructures exist, such as thermal or laser nanowelding, thermal nTP, and others. By incorporating an optimal process for fabricating 3D nanostructures, reducing the manual stacking steps, which introduce misalignment, can further minimize alignment issues. By following this modified sequence, misalignment can be minimized, as this approach requires only a single floating step.

In conclusion, the WF-nTP technology, with its exceptional versatility, demonstrated significant potential for application in various fields, such as agriculture, optics, smart fabrics, and skin electronics. By eliminating the need for toxic substances or adhesives that could alter the natural properties of the substrate, WF-nTP is particularly well suited for biosurfaces, such as plant leaves, human skin, and organ monitoring systems, which are highly sensitive to external factors. Considering that a biointerface is essential for detecting biosignals without interference, WF-nTP is expected to offer distinct advantages for bioelectronics. Thus, this technology has significant potential for a wide range of applications, paving the way for breakthroughs in bioelectronics, environmental monitoring, and smart agriculture.

## Methods

### Sample fabrication

(1) **Nanopatterned Mold Fabrication:** A Si master with various mesh structures was designed using krypton fluoride lithography to prepare a sacrificial nanopatterned polymer mold. RM-311 polyurethane UV-curable resin (Minuta Technology Co., Korea) was poured onto the prepared Si master mold and sealed with a UV-transparent polyethylene terephthalate (PET) film. Proper pressure was applied to the PET film using a commercial handy roller to ensure that the resin fully covered the nanopatterned master mold. The resin was exposed to UV light at a peak wavelength of 365 nm for 90 s before being separated from the master. Various types of nanopatterned molds can be fabricated by following this procedure using different Si master molds, as shown in Supplementary Fig. 2.

(2) **Floating Nanostructures on Water:** From the mesh type Si master mold, the dot type PUA mold was replicated through nanoimprinting process. Target materials, including Au, Pd, Pt, and Ni, were deposited on the nanopatterned mold using an e-beam evaporation system (Daeki Hi-Tech Co., Korea). Then, the top dot side of target materials was removed. Previously, the authors developed a metal-independent nTP technique using trichloro(1H,1H,2H,2H-perfluorooctyl) silane as the SAM[30]. A SAM layer, used as an adhesive to remove the top dot side of the target material, was spin-coated onto the wafer. The target material was then pressed onto the SAM-coated wafer on a hot plate at 150 °C. After 4 min, the mold was released from the wafer. During this process, the target materials on the top dot side were removed, as depicted in Supplementary Fig. 3. Afterwards, the mold was subjected to a 20-minute $O_2/CF_4$ plasma treatment at 100 W power, with an $O_2$ flow rate of 98 sccm and $CF_4$ at 20 sccm, to selectively etch the PUA mold, leading to the suspension of the target material on the bottom mesh side.

(3) **Nanotransfer Printing on Various Substrates:** The plasma-etched mold with the target material was immersed in a water bath. After plasma etching, the target material was suspended, creating a gap between the target material and mold that facilitated water penetration. Subsequently, the nanomesh was separated from the PUA mold and floated on the water surface. The water-floating nanomesh could be transferred to various surfaces, such as glass slides, optical lenses, plant leaves, and fruits, by simply scooping it up. The nanomesh achieved conformal contact when the remaining water completely evaporated.

Supplementary Fig. 1 illustrates these three steps. All chemical agents and EtOH (≥99.50% purity) were purchased from Sigma-Aldrich (USA). Optical lenses were purchased from Edmund Optics (USA). All fruits and plant leaves were purchased from a local market in Daejeon, Korea.

### Characterization

A focused-ion beam integrated scanning electron microscope (SEM, Helios Nanolab™, FEI, Netherlands) was used to investigate the cross-section images with varying plasma etching times and verify the conformal transfer of the mesh to the leaf surface. Ultra-high-resolution SEM combined with energy-dispersive spectroscopy (EDS, SU8230, Hitachi, Japan) was employed to measure the morphology of various nTP substrates and transferred mesh structures. The radius of curvature of the optical lens was measured using a radius indicator (Dongguan Yongchuan Equipment Co., Ltd, China). A digital multimeter (Fluke 15B + , Fluke Corporation, USA) was used to measure the electrical resistance of the mesh on the curved lens based on the Au thickness. The water contact angle on the glass slide and leaf and the water/EtOH mixture contact angle on the back side of the leaf were measured using contact angle detection equipment (KRÜSS Scientific, Germany).

### Electrical impedance spectroscopy measurement

Electrical impedance spectroscopy (EIS) was performed on plant leaves using both a conventional metal clip electrode and a single-layer Au mesh electrode transferred via WF-nTP. The measurements, conducted over a frequency range of 1 Hz to $10^5$ Hz with 0.1 V using a commercial impedance analyzer (PalmSens4, PalmSens, Netherlands) compared impedance magnitude and phase angle under identical conditions.

### Pesticide residue conversion

The surface residue density $\rho_{surf}$ is defined as the applied mass per wetted surface area and was calculated as:

$$\rho_{surf}[\mu g\, cm^{-2}] = (C_{sol}[mM] \times V_{applied}[\mu L] \times 0.24043)/A_{wet}[cm^2]$$

where, 0.24043 converts mM and µL to µg using the molar mass of thiram (M = 240.43 g $mol^{-1}$). $C_{sol}$ is the thiram concentration in solution, $V_{applied}$ is the dispensed volume, and $A_{wet}$ is the wetted area measured.

### Raman measurement

R6G and thiram were purchased from Sigma-Aldrich (USA) and dissolved in EtOH and water, respectively. R6G solutions with concentrations ranging from $10^{-3}$ M to $10^{-6}$ M and thiram solutions with concentrations of $10^{-3}$ M and $10^{-4}$ M were prepared. R6G and thiram solution were drop-casted on the multilayered mesh structure (27 µl$cm^{-2}$) and dried. The Raman shift was collected for 60 s using a dispersive Raman spectrometer (ARAMIS, Horiba, France) equipped with a 785 nm laser. Gratings with 1200 grooves $mm^{-1}$ and a × 50 microscope were used to focus the laser onto the sample.

### Gas-sensing measurement

Gas-sensing experiments were performed in a sealed chamber equipped with a probe. Real-time resistance was monitored using a Keithley 2635 B source meter (Tektronix, Inc., USA). Mass flow controllers (MFCs) were used to control the gas concentration and flow rate. The source meter and MFCs were managed using the LabVIEW interface. During the tests, the resistance change was recorded by alternating the flow of hydrogen gas and nitrogen at 1000-second intervals. Selectivity

tests were performed using nitrogen dioxide, carbon monoxide, and hydrogen sulfide.

## Data availability

All data that support the main findings are available in the main text and the Supplementary Information. Any additional requests for information can be directed to, and will be fulfilled by, the corresponding authors. Source data are provided with this paper.

## References


1. Ahn, J. et al. Nanoscale three-dimensional fabrication based on mechanically guided assembly. *Nat. Commun.* **14**, 833 (2023).
2. Han, H. J. et al. Synergistic integration of chemo-resistive and SERS sensing for label-free multiplex gas detection. *Adv. Mater.* **33**, e2105199 (2021).
3. Ko, J. et al. Nanotransfer printing on textile substrate with water-soluble polymer nanotemplate. *ACS Nano* **14**, 2191–2201 (2020).
4. Gu, J. et al. Self-powered strain sensor based on the piezo-transmittance of a mechanical metamaterial. *Nano Energy* **89**, 106447 (2021).
5. Gu, J. et al. Auxetic kirigami structure-based self-powered strain sensor with customizable performance using machine learning. *Nano Energy* **130**, 110124 (2024).
6. Wu, L. et al. Beetle-inspired gradient slant structures for capacitive pressure sensor with a broad linear response range. *Adv. Funct. Mater.* **34**, 2312370 (2024).
7. Ko, J. et al. Metasurface-embedded contact lenses for holographic light projection. *Adv. Sci. (Weinh.)* **11**, e2407045 (2024).
8. Ahn, J. et al. Nanotransfer-on-things: from rigid to stretchable nanophotonic devices. *ACS Nano* **17**, 5935–5942 (2023).
9. Ko, J. et al. Biocompatible nanotransfer printing based on water bridge formation in hyaluronic acid and its application to smart contact lenses. *ACS Appl Mater. Interfaces* **13**, 35069–35078 (2021).
10. Jeong, J. W. et al. 3D cross-point plasmonic nanoarchitectures containing dense and regular hot spots for surface-enhanced raman spectroscopy analysis. *Adv. Mater.* **28**, 8695–8704 (2016).
11. Zhao, Z. J. et al. Large-area nanogap-controlled 3D nanoarchitectures fabricated via layer-by-layer nanoimprint. *ACS Nano* **15**, 503–514 (2021).
12. Zhao, Z. J. et al. Shape-controlled and well-arrayed heterogeneous nanostructures via melting point modulation at the nanoscale. *ACS Appl Mater. Interfaces* **13**, 3358–3368 (2021).
13. Li, Z., Fan, Q. & Yin, Y. Colloidal self-assembly approaches to smart nanostructured materials. *Chem. Rev.* **122**, 4976–5067 (2021).
14. Jiang, X., Chen, F., Zhao, S. & Su, W. Recent progress in the CVD growth of 2D vertical heterostructures based on transition-metal dichalcogenides. *CrystEngComm* **23**, 8239–8254 (2021).
15. Mackus, A. J. M., Merkx, M. J. M. & Kessels, W. M. M. From the bottom-up: toward area-selective atomic layer deposition with high selectivity. *Chem. Mater.* **31**, 2–12 (2018).
16. Miao, L. et al. Influence of chemical structures on E-beam lithography performance of polysilsesquioxanes. *ACS Appl Mater. Interfaces* **16**, 51554–51564 (2024).
17. Li, P. et al. Recent advances in focused ion beam nanofabrication for nanostructures and devices: fundamentals and applications. *Nanoscale* **13**, 1529–1565 (2021).
18. Wu, W., Hu, M., Ou, F. S., Li, Z. & Williams, R. S. Cones fabricated by 3D nanoimprint lithography for highly sensitive surface enhanced Raman spectroscopy. *Nanotechnology* **21**, 255502 (2010).
19. Jeong, J. W. et al. High-resolution nanotransfer printing applicable to diverse surfaces via interface-targeted adhesion switching. *Nat. Commun.* **5**, 5387 (2014).
20. Park, T. W. et al. Thermally assisted nanotransfer printing with sub–20-nm resolution and 8-inch wafer scalability. *Sci. Adv.* **6**, eabb6462 (2020).
21. Ahn, J. et al. Illuminating Recent Progress in Nanotransfer Printing: Core Principles, Emerging Applications, and Future Perspectives. *Adv. Sci. (Weinh.)* **11**, e2303704 (2024).
22. Ahn, J. et al. Morphology-controllable wrinkled hierarchical structure and its application to superhydrophobic triboelectric nanogenerator. *Nano Energy* **85**, 105978 (2021).
23. Ha, J. H. et al. Nanotransfer printing of functional nanomaterials on electrospun fibers for wearable healthcare applications. *Adv. Funct. Mater.* **34**, 2401404 (2024).
24. Zhao, Z. J. et al. 3D layer-by-layer Pd-containing nanocomposite platforms for enhancing the performance of hydrogen sensors. *ACS Sens* **5**, 2367–2377 (2020).
25. Zhao ZJ, Shin SH, Choi DG, Park SH, Jeong JH. Shape-controlled 3D periodic metal nanostructures fabricated via nanowelding. *Small* **14**, (2018).
26. Gupta, V., Snow, R., Wu, M. C., Jain, A. & Tsai, J. C. Recovery of stiction-failed MEMS structures using laser-induced stress waves. *J. Microelectromech. Syst.* **13**, 696–700 (2004).
27. Rogers, J. W. & Phinney, L. M. Process yields for laser repair of aged, stiction-failed, MEMS devices. *J. microelectromech. Syst.* **10**, 280–285 (2002).
28. Tas, N., Sonnenberg, T., Jansen, H., Legtenberg, R. & Elwenspoek, M. Stiction in surface micromachining. *J. Micromech. Microeng.* **6**, 385 (1996).
29. Zhuang, Y. X. & Menon, A. On the stiction of MEMS materials. *Tribology Lett.* **19**, 111–117 (2005).
30. Hwang, S. H. et al. Covalent bonding-assisted nanotransfer lithography for the fabrication of plasmonic nano-optical elements. *Nanoscale* **9**, 14335–14346 (2017).
31. Miyamoto, A. et al. Inflammation-free, gas-permeable, lightweight, stretchable on-skin electronics with nanomeshes. *Nat. Nanotechnol.* **12**, 907–913 (2017).
32. Kim, J. H. et al. Tensile testing of ultra-thin films on water surface. *Nat. Commun.* **4**, 2520 (2013).
33. Kim, J. J., Allison, L. K. & Andrew, T. L. Vapor-printed polymer electrodes for long-term, on-demand health monitoring. *Sci. Adv.* **5**, eaaw0463 (2019).
34. Nath, S. Prediction of surface tension of highly nonideal aqueous-organic mixtures as a function of composition by a partitioning model between surface and bulk phases and use of partial molar surface areas. *J. Mol. Liq.* **262**, 255–260 (2018).
35. Dreischuh T, et al. Applications of ultrafast lasers in materials processing: fabrication on self-cleaning surfaces and scaffolds for tissue engineering. In: *15th International School on Quantum Electronics: Laser Physics and Applications*) (2008).
36. Schneider, L., Laustsen, M., Mandsberg, N. & Taboryski, R. The Influence of Structure Heights and Opening Angles of Micro- and Nanocones on the Macroscopic Surface Wetting Properties. *Sci. Rep.* **6**, 21400 (2016).
37. Yong J, Yang Q, Hou X, Chen F. Nature-Inspired Superwettability Achieved by Femtosecond Lasers. *Ultrafast Science* **2022**, (2022).
38. Cho SH, Baek KM, Jung YS. Scalable Nanofabrication of Plasmonic Nanostructures for Trace-Amount Molecular Sensing Based on Surface-Enhanced Raman Spectroscopy (SERS). In: *Smart Sensors and Systems: Technology Advancement and Application Demonstrations* (eds Liu Y, Lin Y-L, Kyung C-M, Yasuura H). Springer International Publishing (2020).
39. de Barros, A. et al. Dynamic behavior of surface-enhanced raman spectra for rhodamine 6 G interacting with gold nanorods: implication for analyses under wet versus dry conditions. *ACS Appl. Nano Mater.* **3**, 8138–8147 (2020).
40. Lin, S. et al. Rapid and sensitive SERS method for determination of Rhodamine B in chili powder with paper-based substrates. *Anal. Methods* **7**, 5289–5294 (2015).

41. Wang, J. et al. Ultrasensitive SERS detection of rhodamine 6 G and p-nitrophenol based on electrochemically roughened nano-Au film. *Talanta* **210**, 120631 (2020).
42. Chen, J. et al. Flexible and adhesive surface enhance raman scattering active tape for rapid detection of pesticide residues in fruits and vegetables. *Anal. Chem.* **88**, 2149–2155 (2016).
43. Chen, Z. et al. SERS detection of triazole pesticide residues on vegetables and fruits using Au decahedral nanoparticles. *Food Chem.* **439**, 138110 (2024).
44. Jiang, J. et al. Surface-enhanced raman scattering detection of pesticide residues using transparent adhesive tapes and coated silver nanorods. *ACS Appl Mater. Interfaces* **10**, 9129–9135 (2018).
45. Kesava Rao V, et al. An Ultralow-Cost, Durable, Flexible Substrate for Ultrabroadband Surface-Enhanced Raman Spectroscopy. *Adv. Photonics Res.* **5**, 2300291 (2023).
46. Kitahama, Y. et al. Place & Play SERS: sample collection and preparation-free surface-enhanced Raman spectroscopy. *Anal. Methods* **15**, 1028–1036 (2023).
47. Horiue, H., Sasaki, M., Yoshikawa, Y., Toyofuku, M. & Shigeto, S. Raman spectroscopic signatures of carotenoids and polyenes enable label-free visualization of microbial distributions within pink biofilms. *Sci. Rep.* **10**, 7704 (2020).
48. Dao TC, Luong TQN, Cao TA, Kieu NM. High-sensitive SERS detection of thiram with silver nanodendrites substrate. *Adv. Nat. Sci.: Nanosci. Nanotechnol.* **10**, (2019).
49. Pu, H., Huang, Z., Xu, F. & Sun, D. W. Two-dimensional self-assembled Au-Ag core-shell nanorods nanoarray for sensitive detection of thiram in apple using surface-enhanced Raman spectroscopy. *Food Chem.* **343**, 128548 (2021).
50. Cho S, et al. Wireless, battery-free, optoelectronic diagnostic sensor integrated colorimetric dressing for advanced wound care. *Adv. Funct. Mater.* **34**, 2316196 (2024).
51. Ha JH, et al. Multifunctional micro/nanofiber based-dressing patch with healing, protection, and monitoring capabilities for advanced wound care. *Adv. Mater. Technol.* **8**, (2023).

## Acknowledgements

I.P. was supported by the National Research Foundation of Korea (NRF) grant funded by the Korean government (MSIT) (No. 2021R1A2C3008742). J-H. J. was supported by Alchemist Project grant funded by Korea Evaluation Institute of Industrial Technology (KEIT) & the Korea Government (MOTIE) (Project number: 1415179744, 20019169). J. A. was supported by Korea Evaluation Institute of Industrial Technology (KEIT) grant funded by the Korea government (MOTIE, Grant No. RS-2022-00154781, Development of large-area wafer-level flexible/stretchable hybrid sensor platform technology for form-factor-free highly integrated convergence sensor).

## Author contributions

B-H. K. and I.P. led the development of the concepts, designed the experiments, and interpreted the results; B-H. K. led the experimental work from J-H. H., Y.K., and B.K.; D.L., S.J. and S.H. supported the simulation of design; J.A., J-H. J., and I.P. directed the project.

## Competing interests

The authors declare no competing interests.

## Additional information

**Supplementary information** The online version contains supplementary material available at https://doi.org/10.1038/s41467-026-70902-5.

**Correspondence** and requests for materials should be addressed to Junseong Ahn, Jun-Ho Jeong or Inkyu Park.

**Peer review information** *Nature Communications* thanks Xiaodong Chen, Yan-Ling Liu, Yan Wang and the other, anonymous, reviewer(s) for their contribution to the peer review of this work. A peer review file is available.

**Reprints and permissions information** is available at http://www.nature.com/reprints

**Publisher's note** Springer Nature remains neutral with regard to jurisdictional claims in published maps and institutional affiliations.

**Open Access** This article is licensed under a Creative Commons Attribution-NonCommercial-NoDerivatives 4.0 International License, which permits any non-commercial use, sharing, distribution and reproduction in any medium or format, as long as you give appropriate credit to the original author(s) and the source, provide a link to the Creative Commons licence, and indicate if you modified the licensed material. You do not have permission under this licence to share adapted material derived from this article or parts of it. The images or other third party material in this article are included in the article's Creative Commons licence, unless indicated otherwise in a credit line to the material. If material is not included in the article's Creative Commons licence and your intended use is not permitted by statutory regulation or exceeds the permitted use, you will need to obtain permission directly from the copyright holder. To view a copy of this licence, visit http://creativecommons.org/licenses/by-nc-nd/4.0/.

© The Author(s) 2026